Nanoscale Advances

ROYAL SOCIETY OF CHEMISTRY

PAPER

View Article Online
View Journal | View Issue

Cite this: *Nanoscale Adv.*, 2024, **6**, 2469

In vitro profiling and molecular dynamics simulation studies of berberine loaded MCM-41 mesoporous silica nanoparticles to prevent neuronal apoptosis†

Anurag Kumar Singh, ‡[a] Snigdha Singh,‡[a] Tarun Minocha,[b] Sanjeev Kumar Yadav,[b] Reema Narayan,[c] Usha Yogendra Nayak,[c] Santosh Kumar Singh*[a] and Rajendra Awasthi *[d]

Neuronal loss in Alzheimer's disease has been reported to display features of apoptosis, pyroptosis (programmed necrosis), or necroptosis. This study thoroughly examines the production and characterization of MCM-41 based berberine (BBR)-loaded porous silica nanoparticles (MSNs) by a modified Stöber method, focusing on their possible role in inhibiting the apoptotic process. Particle size, polydispersity index, morphology, drug loading, zeta potential, entrapment efficiency, and drug release were examined. The formulation was analyzed using various spectroscopic techniques. The surface area was computed by the Brunauer–Emmett–Teller plot. Computational models were developed for molecular dynamics simulation studies. A small PDI value indicated an even distribution of particles at nanoscale sizes (80–100 nm). Results from XRD and SEAD experiments confirmed the amorphous nature of BBR in nanoparticles. Nanoparticles had high entrapment (75.21 ± 1.55%) and drug loading (28.16 ± 2.5%) efficiencies. A negative zeta potential value (−36.861.1 mV) indicates the presence of silanol groups on the surface of silica. AFM findings reveal bumps due to the surface drug that contributed to the improved roughness of the MSNs–BBR surface. Thermal gravimetric analysis confirmed the presence of BBR in MSNs. Drug release was controlled by simple diffusion or quasi-diffusion. Molecular dynamics simulations confirmed the existence of diffused drug molecules. Cellular studies using SH-SY-5Y cells revealed dose-dependent growth inhibition. Fragmented cell nuclei and nuclear apoptotic bodies in DAPI-stained cells exposed to nanoparticles showed an increase in apoptotic cells. Flow cytometry analysis demonstrated a lower red-to-green ratio in SH-SY-5Y cells treated with nanoparticles. This suggests improved mitochondrial health, cellular viability restoration, and prevention of the apoptotic process. This study provides essential data on the synthesis and potential of MSNs loaded with BBR, which may serve as a viable therapeutic intervention for conditions associated with apoptosis.

Received 22nd December 2023
Accepted 27th March 2024

DOI: 10.1039/d3na01142a

rsc.li/nanoscale-advances

1 Introduction

Dementia has affected more than 55 million individuals worldwide in different ways, depending on the underlying causes and other health conditions. Dementia is the seventh-leading cause of death.[1] It is anticipated that after cardiovascular diseases, neurodegenerative disorders are projected to become the primary cause of death, surpassing cancer.[2,3] The estimated annual cost of neurodegenerative disorder treatment in the U.S.A. is >800 billion US dollars.[4] Lack of diagnostic biomarkers and challenging identification of drug targets are the major hurdles to effective management of neurodegenerative diseases.[4] The endothelium of brain capillaries creates an epithelial-like barrier known as the blood–brain barrier that limits drug diffusion throughout the brain.[5]

Formulation scientists are paying close attention to nanoparticle development because of their large and tunable pore size, and enhanced cellular transport for site-specific administration, which results in superior therapeutic intervention over traditional treatments.[6,7] In recent years, substantial

[a]*Centre of Experimental Medicine & Surgery, Institute of Medical Sciences, Banaras Hindu University, Varanasi 221005, Uttar Pradesh, India. E-mail: singhsk71@yahoo.com; Tel: +91-9415389046*

[b]*Department of Zoology, Institute of Science, Banaras Hindu University, Varanasi 221005, India*

[c]*Department of Pharmaceutics, Manipal College of Pharmaceutical Sciences, Manipal Academy of Higher Education, Manipal, 576104, Karnataka, India*

[d]*Department of Pharmaceutical Sciences, School of Health Sciences & Technology, UPES University, Dehradun 248007, Uttarakhand, India. E-mail: rajendra.awasthi@ddn.upes.ac.in; awasthi02@gmail.com; Tel: +91-9495234530*

† Electronic supplementary information (ESI) available. See DOI: https://doi.org/10.1039/d3na01142a

‡ These authors contributed equally.

advancements have been observed in several therapeutic carrier systems. Mobil Crystalline Material No. 41 (MCM-41) mesoporous silica nanoparticles (MSNs) are gaining significant interest in drug delivery. The Stöber method is regarded as the most efficient technique for producing monodisperse silica spheres when compared to traditional methods such as the flame synthesis and micro-emulsion methods. The Stöber method offers a versatile chemical pathway that yields compounds that are well-dispersed, highly pure, and chemically reactive. The condensation and hydrolysis can be carried out at lower temperatures than in traditional methods.[8] MSNs excel as nanocarriers due to tunable pore characteristics, high drug loading, chemical stability, biocompatibility, facile surface functionalization, controlled release, cargo versatility, multimodal imaging potential, ease of production, and prolonged circulation time, making them promising for diverse biomedical applications.[9] MSNs are promising for blood storage due to their antioxidant properties, however their large surface area may cause protein adsorption and impact biocompatibility.[10] Silica nanoparticles, such as MSNs, function as permeation enhancers, especially in overcoming biological barriers like tight junctions in the gut. The surface roughness of nanoparticles is vital in determining their interaction with barriers like the blood–brain barrier, affecting adhesion and protein interactions.[11] We previously described the synthesis of silica nanoparticles loaded with berberine in our research. The nanoparticles showed a significant inhibitory effect on acetylcholinesterase in mice stimulated with scopolamine.[3] Expanding on these findings, our current study investigates the therapeutic efficacy of the developed formulation. Through *in vitro* analysis, we focus on the toxicity profile, mitochondrial health, cellular viability restoration, and potential prevention of the apoptotic process.

Berberine, an isoquinoline alkaloid, inhibits the Jun aminoterminal kinases pathway and apoptotic signaling pathway/Akt/2 survival/ERK1/GSK3β/caspase-3 activity. It is obtained from the stem and root of the *Berberis* species. The neuroprotective effect of BBR is associated with suppression of the Akt/ERK1/2 survival/apoptotic signaling pathway/GSK3/caspase-3 and Jun aminoterminal kinase pathways.[12] Its low oral bioavailability (0.36% in humans and 0.68% in animal models) is caused by rapid hepatic clearance[13,14] or the interaction of BBR with P-glycoprotein pumps.[15] The development of MSNs loaded with BBR holds significant importance for advancing drug delivery systems. This approach enhances the bioavailability and stability of BBR through controlled release from MSNs. The significance lies in achieving enhanced solubility and stability of BBR, optimizing therapeutic efficacy and the biocompatibility of silica.

Systemic safety of the developed therapeutic system includes the biocompatibility of the delivery system and safety of the drug dispersed throughout the body.[16] BBR was passively loaded into MSNs synthesized by the Stöber process (MSNs–BBR). MSNs–BBR were characterized for zeta potential, polydispersity index, particle size, entrapment efficiency, morphology, drug loading, specific surface area, porosity, and drug release using various spectroscopic techniques. Molecular dynamics studies were conducted to calculate the diffusion coefficient of BBR for analyzing its release profile. To ascertain the cytotoxic behaviour of synthesised MSNs–BBR, measurements of cell viability, apoptosis, and neuronal-health were performed using the neuroblastoma cell line SH-SY-5Y. After drug therapy, morphological changes were observed in the 4′,6-diamidino-2-phenylindole (DAPI) stained nucleus.

2 Materials and methods

2.1. Materials

Indian Herbs Extractions (Uttarakhand, India) provided BBR. Hydrochloric acid (37%) and dimethyl sulfoxide (DMSO) were purchased from S.D. Fine Chem, India. Tetraethylorthosilicate (TEOS 99%) and hexadecyl trimethyl ammonium bromide (CTAB ≥99%) were obtained from SRL Chemicals, India. CF300-Cu carbon-coated TEM grids were obtained from EMS (Hatfield, Pennsylvania, USA). Acetic acid, sodium dihydrogen phosphate, ammonium chloride, disodium hydrogen phosphate, and potassium chloride were received from Sisco Research Labs, Mumbai, India. Streptomycin, penicillin, trypsin-EDTA, and foetal bovine serum (FBS) were purchased from Gibco (USA). MTT was procured from Sisco Research Laboratory, India. DAPI was obtained from Himedia, Mumbai, India. Methanol, acetone, DMSO, and JC-1 were procured from Sigma-Aldrich, St. Louis, USA. An Alexa Fluor 488 Annexin V/dead cell apoptosis kit was procured from ThermoFisher Scientific, MA, USA. Cell culture flasks (T-25) and cell culture plates of various dimensions (6, 12, and 96 wells) were purchased from Genetix Biotech Asia (New Delhi, India).

2.2. Methods

2.2.1. Mesoporous silica nanoparticle preparation and drug loading. The modified Stöber technique was used to synthesize mesoporous silica nanoparticles (MSNs) (Fig. 1).[16–18] 1000 mg of CTAB was added to deionized water (480 mL) containing 2.5 M NaOH solution (2 mL) at 80 °C and stirred for 30 min. After 30 min of mixing, the temperature was maintained at 25 °C, and TEOS (5 mL) was added (1 mL min^{-1}) followed by stirring at 700 rpm for 3 h. Centrifugation was done for 15 min at 10 000 rpm. The particles were collected, dried, and then refluxed in an acidified ethanolic solution for 6 h. Organic compounds and surfactants were removed following 6 h calcination at 550 °C. For passive drug loading, MCM-41 (1 mg) was added to 1 mL of BBR solution (1 mg mL^{-1}) and stirred for 4 h at 25 ± 1 °C and 350 rpm using a magnetic stirrer. Centrifugation was done at 5000 rpm for 30 min. BBR loaded particles (MSNs–BBR) were collected, rinsed twice with distilled water to remove the free drug, and dried in a desiccator.[3]

2.2.2. Characterization of MSNs–BBR

2.2.2.1. Particle size, zeta potential, polydispersity index, entrapment, and drug loading efficiency. The hydrodynamic diameter, polydispersity index (PDI), and zeta potential of MSNs–BBR and MCM-41 were determined using dynamic light scattering (DLS) measurements using a Zetasizer (NanoZS, Malvern Instruments, Malvern, United Kingdom). Sample

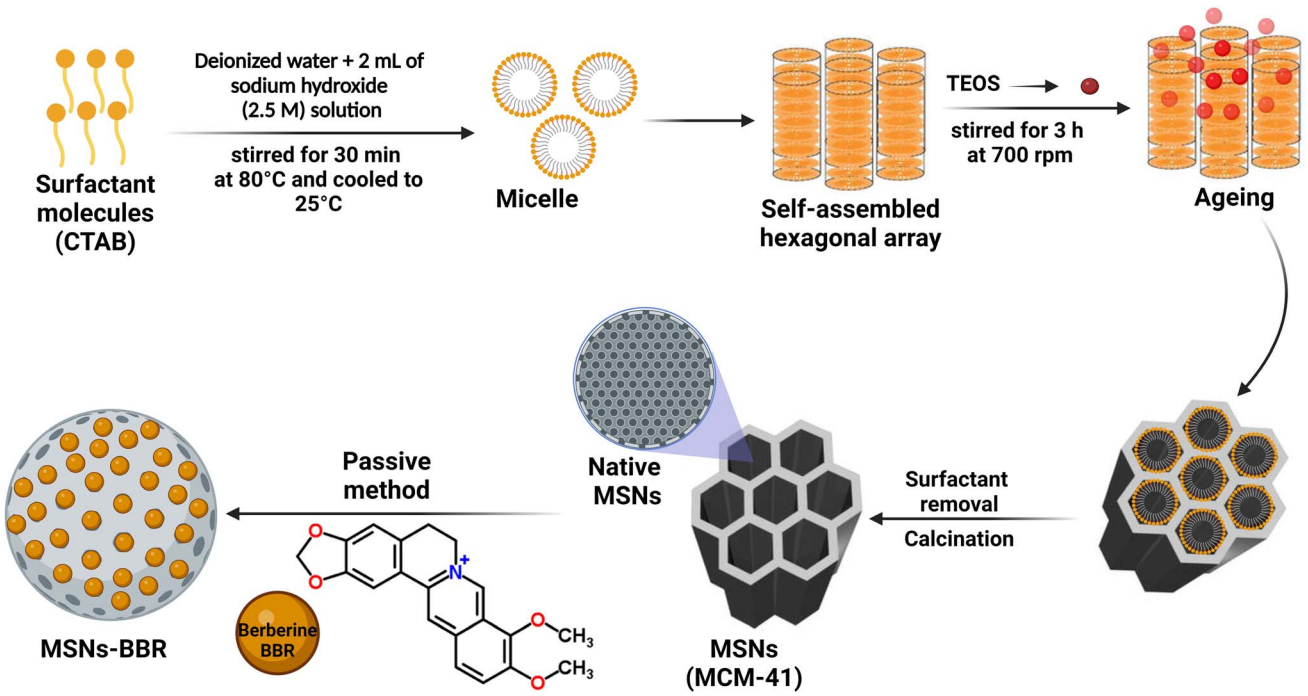

Fig. 1 Synthesis of berberine-loaded mesoporous silica nanoparticles by a modified Stober method.

dispersion was prepared using Milli-Q water. A scattering angle of 45° to 150° with 8° intervals and a refractive index of 1.10 were used to carry out DLS analysis. Sample sonication was done in a probe sonicator. The hydrodynamic diameter of particles was recorded based on the cumulated intensity distribution. Zeta potential was measured following laser doppler velocimetry (5 measurements per sample in duplicate). The investigation of the size distribution was carried out with the assistance of a Zetasizer that had a diode laser that was set to run at 659 nm. Three independent measurements were taken of each variable.[3]

To calculate the fraction of loaded BBR, the quantity of free BBR in the supernatant was analyzed. A sample containing 5 mg of MSNs–BBR was diluted to 5 mL with Milli-Q water and centrifuged at 8000 rpm for 30 minutes. The supernatant was analyzed at 345 nm using a Labtronics UV spectrophotometer (LT-2800) to determine the amount of free BBR. The percentage of drug loading and entrapment were calculated using the following equations:[3,19]

$$\text{Drug loading}(\%) = \frac{\text{Theoretical amount of drug}}{\text{Weight of nanoparticles}} \times 100$$

$$\text{Entrapment efficiency}(\%) = \frac{\text{Actual amount of drug in nanoparticles}}{\text{Theoretical amount of drug taken}} \times 100$$

2.2.2.2. Morphological characterization. MSNs-–BBR and MCM-41 particles were analyzed using a high-resolution nova nano scanning electron microscope (HRSEM) (SEM 450, FEI, USA), a transmission electron microscope (TEM) (G2 T20 Technai, USA), and a NTEGRA prima atomic force microscope (AFM, NT-MDT Service & Logistics Ltd, Ireland). Gold-coated samples were air-dried before placed on a silica wafer for SEM analysis and images were captured at 8–10 kV. Working distance and spot size were 4.4 mm and 200 μ, respectively. For TEM imaging, particles were put into water (1 mg mL^{-1}) and sonicated for 30 minutes. Sample dispersion (5 mL) was transferred to the TEM grids, dried at 40 °C for 12 h, and examined at 200 kV. Images were captured by a 135 mm CCD camera (charge-coupled device) at 200 kV. A spin coater was used to evenly spread a drop of sample dispersion across a thin glass slide for AFM analysis. Images were captured at 256 × 256 pixels resolution, a nominal force constant of 40 N m^{-1}, 300 kHz cantilever frequency, and at room temperature.[3] A TEAM Pegasus integrated energy dispersive spectroscopy system was used for sample analyses with a Nova Nano SEM 450 (FEI, P.T.E., Singapore). The samples were dried at 40 °C for 20 min. The gold coating of the samples was done using a SEM sputter coater. The images were captured by a CCD camera at 200 kV.

2.2.2.3. Infra-red spectroscopy. An Attenuated Total Reflectance spectrophotometer (L160000A, ATR, PerkinElmer, USA) was used to record infrared spectra from 4000 cm^{-1} to 400 cm^{-1} with a resolution of 4 cm^{-1}.

2.2.2.4. Powder X-ray diffraction analysis. X-ray diffraction (XRD) study of BBR, MCM-41 (low angle), MSNs–BBR, and BBR: MCM-41 physical mixture (1 : 1 w/w ratio) was done using an X-ray powder diffractometer (D/max-2550, Rigaku Co., Tokyo, Japan). Samples were analyzed using CuKα radiation at 40 kV voltage, 200 mA current, and 1.54 Å wavelength. The sample analysis was done from 0 to 80° of 2θ angles.[18,20]

2.2.2.5. X-ray photoelectron spectroscopy analysis. A PHI 5000 Versa Probe III from ULVAC-PHI Inc., Japan, fitted with

a monochromatic Al K radiation source, was used for X-ray photoelectron spectroscopy (XPS). XPS spectra of MCM-41, BBR, and MSNs–BBR were recorded. Calibration was done by using the C 1s peak at 284.5 eV as an internal standard to identify the characteristic binding energies of elements on the BBR loaded silica nanoparticle. The XPS scanning was conducted for important elements such as C, N, O, and Si.[21]

2.2.2.6. Thermogravimetric analysis. A thermogravimetric analyzer was used to measure the 5 mg sample's weight loss (TGA-50, Shimadzu, Japan). The temperature range of 25 to 700 °C was measured at a rate of 10 °C per min.

2.2.2.7. Porosity and specific surface area of MSNs. A Micromeritics Tristar II system (Tristar 3020, Micromeritics-II, Norcross, GA, USA) was used at 196 °C to measure nitrogen physisorption–desorption isotherms. Helium was used to calibrate the dead volume in the sample cell, and nitrogen was used as an adsorbate. Before analysis, MSNs were outgassed (at 120 °C for 12 h) to remove any possible moisture in their pores. Utilizing the Brunauer–Emmett–Teller equation, the specific surface area was determined. Pore size distribution was calculated using the Barrett–Joyner–Halenda method.[22] The amount of N_2 adsorbed at a relative pressure (P/P_0) of 0.99 was used to calculate the total pore volume.

2.2.2.8. In vitro drug release study. Methanolic BBR solution (equivalent to 1000 μg of BBR) was filled in dialysis bags (capacity 1.61 mL cm^{-1}, cut off molecular weight 5000 Dalton, −50Av. flat, width 22.54 mm, diameter 14.3 mm; Himedia, Mumbai, India). Ten milligrams of the formulation (≈1000 μg BBR) was incubated in dissolution fluid (1 mL) and filled in the dialysis bag. Release studies were carried out using 100 mL each of acidic (pH 4.0) and neutral media (phosphate buffer saline: PBS pH 7.4) separately. Samples (1 mL) were collected at specified intervals, and the sink condition was maintained by the addition of an equal amount of fresh dissolution medium immediately after each sample withdrawal. At 345 nm, the sample was analyzed using a Nanodrop ND1000 Thermo Scientific, UV-visible spectrophotometer (Wilmington, USA). The release profile of BBR from pure BBR solution was also estimated.[3]

The kinetics of drug release was studied using zero and first-order plots. The kinetics of release was further confirmed by Higuchi's model. Korsmeyer-Peppas' model was used to confirm whether the drug diffusion is Fickian or non-Fickian.[23]

2.2.3. Construction of computational models of MCM-41. All the simulations and calculations were carried out using the Materials Science Suite (MS-Suite) 2019–04 of Schrödinger (Schrödinger, LLC, New York). An alpha-silica crystal unit cell was used to create the model MSN structure. A bulk system was created by extending the unit cell in all three directions (4 × 4 × 4). The oxygen-terminated silica slab was created using the slab and interface builder in the Schrodinger-Materials Science Suite, and the hydrogen atoms were added to the surface to neutralize it. The surfaces generated were optimized and exposed to molecular dynamics (MD) simulations for 10 ns, and the structure with the lowest energy was chosen as the final optimized structure and used for further studies.[24] The structure of BBR was generated and optimized using the Ligprep tool. Using the disordered system builder, around 500 BBR molecules were added to each side of the MCM surfaces generated and subjected to MD simulation. The first adsorbed layer was selected following MD. Further, 3400 TIP3P water molecules, 100 molecules each of Na_2HPO_4 and KH_2PO_4, and 50 molecules each of NaCl and KCl were added on each side. The entire system was exposed to the MD simulation for 20 ns, and the diffusion coefficient of BBR was calculated to check the release of BBR.[24]

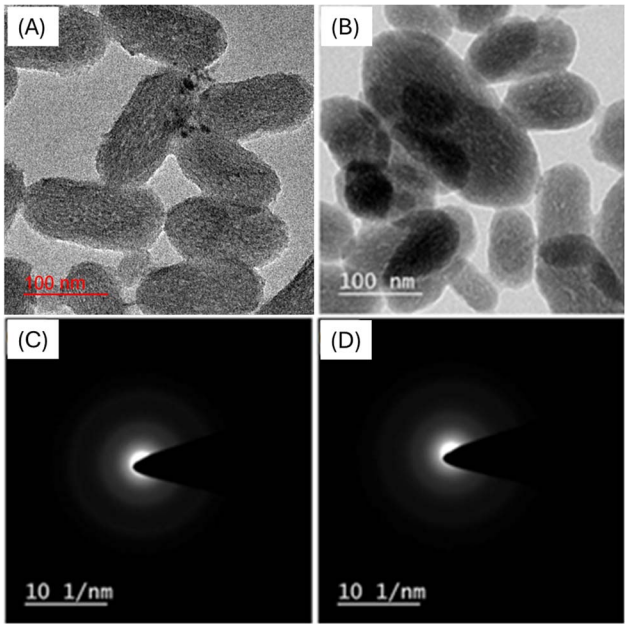

Fig. 2 HRTEM images of (A) MCM-41 and (B) MSNs–BBR at 100 nm, and SAED micrographs of (C) MCM-41 and (D) MSNs–BBR.

2.2.4. Hemolytic assay. A suspension of red blood cells (RBCs) was made according to previously published studies.[25,26] Briefly, the blood sample was obtained from a healthy volunteer, preserved in heparin anticoagulant coated blood vials (Himedia, India), and centrifuged for 20 min at 2600 rpm. RBCs were suspended in 0.9% w/v of normal saline to facilitate cell contact. The samples were made in a normal saline solution with a concentration of 20 ppm. One milliliter of RBC

Table 1 Results of polydispersity index, particle size, zeta potential, entrapment efficiency, and drug loading

Sample code	Particle size (nm)	Zeta potential (mV)	Poly dispersity index (PDI)	Entrapment efficiency (%)	Drug loading (%)
MCM-41	115.5 ± 2.0	−35.18 ± 2.1	0.230 ± 0.01	—	—
MSNs–BBR	137.1 ± 2.4	−38.52 ± 2.2	0.281 ± 0.03	85.23 ± 3.11	33.22 ± 2.6

suspension was mixed with 5 mL of distilled water to achieve complete hemolysis (100% hemolytic). Normal saline (5 mL) was added to RBC suspension (1 mL) to ensure no hemolysis. A mixture of 1 mL of RBC suspension and 4.5 mL of normal saline was added to the half milliliter of MSNs–BBR formulation. Similarly, 0.5 mL MSNs–BBR formulation and half milliliter MCM-41 solution were added to 1 mL RBC suspension and 4.5 mL normal saline. A similar procedure was followed for BBR, and MCM-41 and tubes were allowed to stand for 1 h with gentle shaking and centrifuged for 20 min at 2400 rpm. The absorbance of the supernatant was taken at 540 nm. The following formula was used to determine the percent of hemolysis, with water representing 100% hemolysis.

$$\text{Hemolysis}(\%) = \frac{\text{Absorbance for the sample}}{\text{Absorbance for contr}} \times 100$$

2.3. *In vitro* studies

2.3.1. Cell line maintenance. The human neuroblastoma cell line SH-SY-5Y was purchased from the NCCS, Pune, India. The cells were maintained in a CO_2 chamber and cultured in a 25 cm^2 flask with high glucose DMEM supplemented with 10% FBS, penicillin (100 units per mL), and streptomycin (100 $\mu g\ mL^{-1}$).

2.3.2. Cell viability assay. The cell viability assay was carried out to speculate the cytotoxicity of BBR and MSNs–BBR in the neuroblastoma cell line.[27,28] SH-SY-5Y cells were plated in a 96-well plate and treated with different concentrations of BBR and MSNs–BBR for 24 h. Thereafter, the cells were incubated with MTT (10 μL) for 2 h and subjected to DMSO (100 μL) in each well. Finally, the absorbance was recorded at 570 nm using a microplate reader.

2.3.3. Cell imaging. SH-SY-5Y cells were plated in a 96-well plate and exposed to the indicated concentrations of BBR and MSNs–BBR for 24 h. After the stipulated time, cells were washed with PBS and observed at 10× under a phase contrast microscope (EVOS, Invitrogen, Life Technologies).[29]

2.3.4. Nuclear staining. Nuclear staining was carried out to observe the nuclear alterations following treatment.[30] SH-SY-5Y cells were seeded in a 96-well plate and subjected to the indicated concentrations of BBR and MSNs–BBR for 24 h. Next, the cells were fixed with paraformaldehyde and permeabilized with 100 μL of methanol for 30 min. After 30 min, the cells were washed with PBS, stained using DAPI (2 $\mu g\ mL^{-1}$), and images were taken under a fluorescence microscope (EVOS, Invitrogen, Life Technologies) at 20×.

2.3.5. Annexin V/PI apoptosis staining. Flow cytometric analysis was done to evaluate the percentage of viable, apoptotic, and necrotic cells using an Annexin V-FITC apoptosis kit.[31] Briefly, SH-SY-5Y cells were incubated in a 6-well plate, followed by treatment with the indicated concentration of BBR (50 $\mu g\ mL^{-1}$) and MSNs–BBR (50 $\mu g\ mL^{-1}$) for 24 h. The cells were washed with PBS, harvested, and suspended in 1× annexin binding buffer. The cells were simultaneously stained with annexin V and PI as per the manufacturer's instructions and analyzed by flow cytometry at 10 000 events per sample.

2.3.6. Detection of mitochondrial membrane potential. Flow cytometric analysis was done to assess the mitochondrial membrane potential ($\Delta\Psi$) using the JC-1 staining procedure.[31] Briefly, SH-SY-5Y cells were incubated in a 6-well plate for 24 h followed by treatment with the indicated concentrations of BBR (50 $\mu g\ mL^{-1}$) and MSNs–BBR (50 $\mu g\ mL^{-1}$) for 24 h. After 24 h, the cells were harvested by trypsinization after washing with PBS, stained with JC-1 (10 $\mu g\ mL^{-1}$) at 37 °C for 15 min in the dark, and analyzed by flow cytometry at 10 000 events per sample.

2.4. Statistical analysis

Microsoft Excel (version 2013; Microsoft Corporation, Washington, United States) was used for statistical analysis of *in vitro* drug release data.

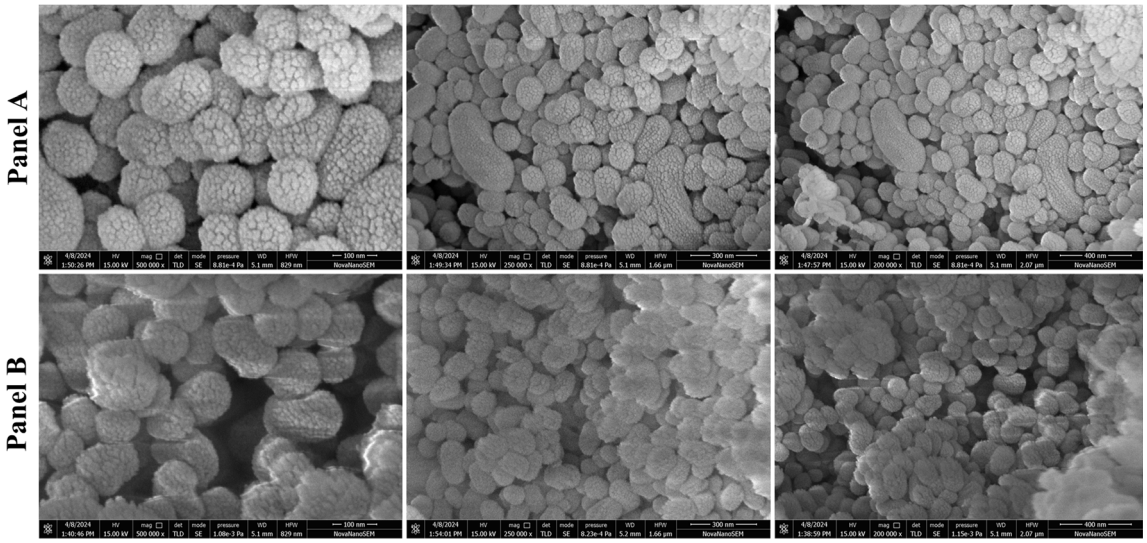

Fig. 3 SEM images of MCM-41 (panel A) and MSNs–BBR (panel B) at 100, 300 and 400 nm.

3 Results and discussion

3.1. Nanoparticle characterization

The results of nanoparticle characterization are presented in Table 1. Samples were analyzed for PDI to determine the width of unimodal size distributions. A PDI value less than 0.7 is considered acceptable.[32] The PDI value should be <0.1 and >1, respectively, for monodisperse and polydisperse size distribution of particles.[33] The PDI value of drug-loaded nanoparticles (0.281 ± 0.03) was higher than that of the MCM-41 particles (0.230 ± 0.01) (Table 1). For good dispersion homogeneity, the PDI value should be small. The MSNs–BBR particles showed a 22 nm increase in particle size (137.1 ± 2.4 nm) in comparison to the MCM-41 particles (115.5 ± 2.0 nm). An increase in particle size may result from the drug being loaded into the particles' pores and the presence of the drug on the surface. These findings are supported by previous studies in which the nanoparticle size increased following drug loading.[34–36] By comparing the data from DLS and TEM studies, it is possible to determine the particle aggregation. Aggregated suspension shows comparatively smaller particles in TEM analysis than DLS.[33] A larger particle size in DLS than in the TEM analysis could be due to the aggregation of particles.[37] The size of prepared MSN–BBR was in the range of 90–110 nm. TEM micrographs of MCM-41 and MSNs–BBR are shown in Fig. 2A and B, respectively. The presence of diffused rings in selected area electron diffraction pattern (SAED) images is indicative of the crystalline nature of the material. The absence of diffused rings in SEAD images confirms the amorphous form of the material (Fig. 2C and 2D).

The percentage of drug entrapment and loading efficiency were 85.23 ± 3.11% and 33.22 ± 2.6%, respectively (Table 1). The electrostatic interaction and hydrogen bonding between BBR and MSNs and the highly porous nature of MCM-41

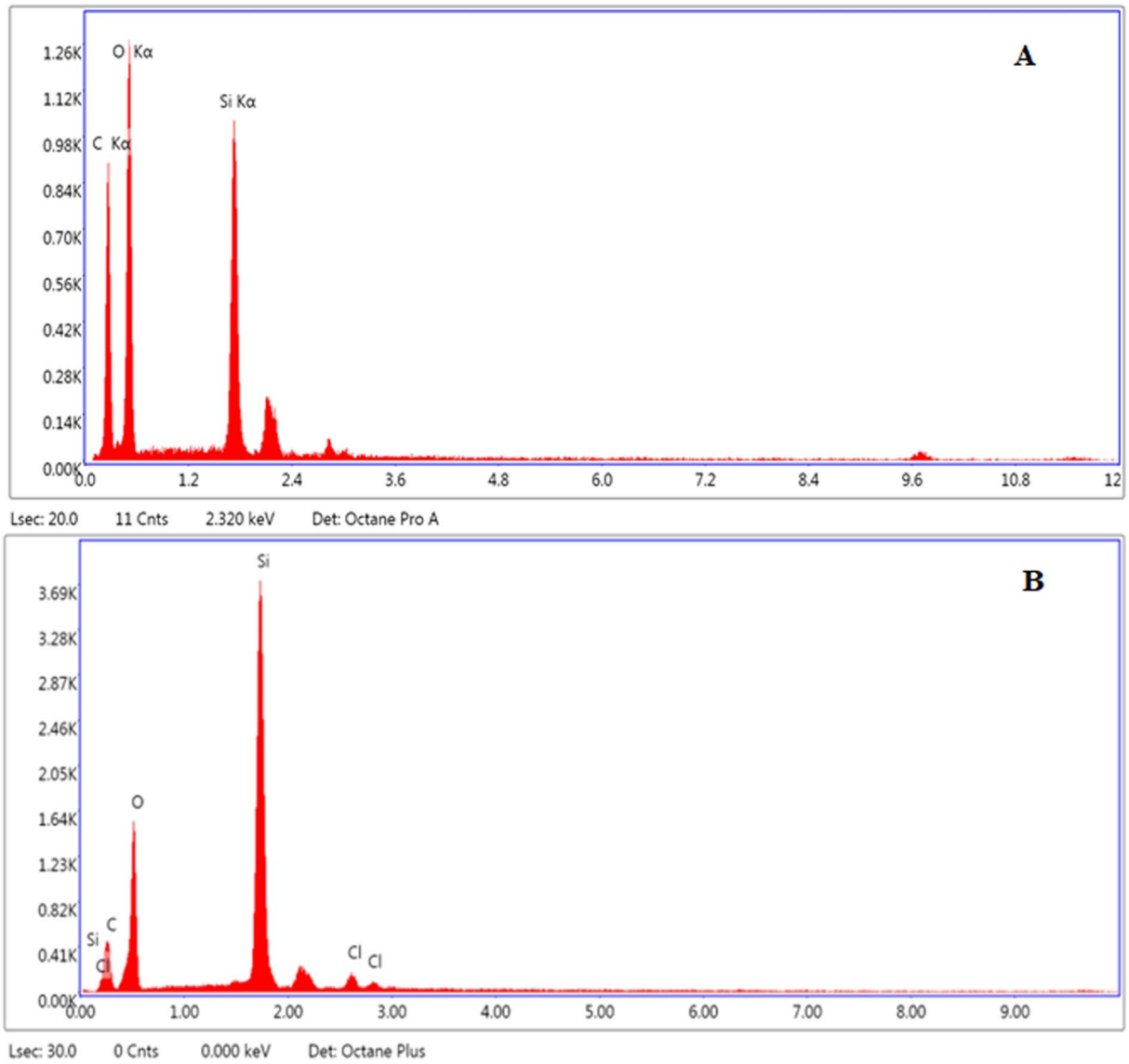

Fig. 4 EDX pattern of (A) MCM-41 and (B) MSNs–BBR.

resulted in high drug loading. The surface charge (−35.18 ± 2.1 mV) of MCM-41 was attributed to the silanol groups on the silica surface.[38] A zeta potential value of −38.52 ± 2.2 mV was recorded after BBR loading into MCM-41. The Zeta potential value reflects the degree of repulsion between particles with the same charge in a dispersion system. When particles have high positive or negative zeta potential values, they repel each other, preventing aggregation. Particles with zeta potentials between ±30 mV are often stable.[39] Nanoparticles with high zeta potential can significantly impact BBB toxicity.[40] Studies have shown that nanoparticles intended for brain delivery typically have negative zeta potentials ranging from −15 to −45 mV.[41,42] SEM images of rod-shaped homogenously distributed MCM-41 and drug loaded nanoparticles are shown in Fig. 3.

Elemental analysis of MCM-41 and drug loaded nanoparticles was carried out to find out the elemental composition, presence of environmental impurities, if any, and weight percentage. Results showed that O, C, and Si were present in all the tested samples. The elemental relative weight percentage obtained was 87.19% C and 12.81% Si (Fig. 4A), and 30.80% O, 18.22% C, 3.07% Cl, and 47.91% Si in MCM-41 and MSNs–BBR, respectively (Fig. 4B).

AFM studies were carried out for the three-dimensional morphological examination of MCM-41 and drug loaded nanoparticles. The mean roughness value (R_a) is determined by taking the arithmetic average of the peak and valley depths from a mean line. The height distribution in relation to the mean line is known as the root mean square roughness (R_q).[43] R_a and R_q of the road-shaped MCM-41 particles were 4.235 nm and 6.076 nm (2D), respectively (Fig. 5A). The root mean square roughness (S_q) and average roughness (S_a) of MCM-41 particles were 86.253 and 98.208 (3D), respectively (Fig. 5B). Smooth surface and high homogeneity were noticed in MCM-41 particles. 2D images showed that the homogeneous MSNs–BBR particles had root mean square (R_a) and roughness average (R_q) values of 10.333 nm and 16.848 nm, respectively (Fig. 5C). The root mean square roughness (S_q) and average roughness (S_a) values of MSNs–BBR were 90.236 nm and 99.686 nm, respectively (3D) (Fig. 5D). The average 2D surface roughness (R_q) of MCM-41 increased from 6.076 nm to 16.848 nm after drug loading in MSNs–BBR. Higher surface roughness suggests the presence of surface drug and effective drug loading.[44]

Absorption bands near 460 cm^{-1}, 802 cm^{-1}, and 1095 cm^{-1} in the FTIR spectrum of MCM-41 reflected Si–O–Si bending, Si–O–Si asymmetric stretching, and Si–O–Si symmetric stretching, respectively. The peak at 1647 cm^{-1} confirmed the presence of –OH bending vibration of physiosorbed water molecules in silica. The peak of Si–OH stretching was recorded near

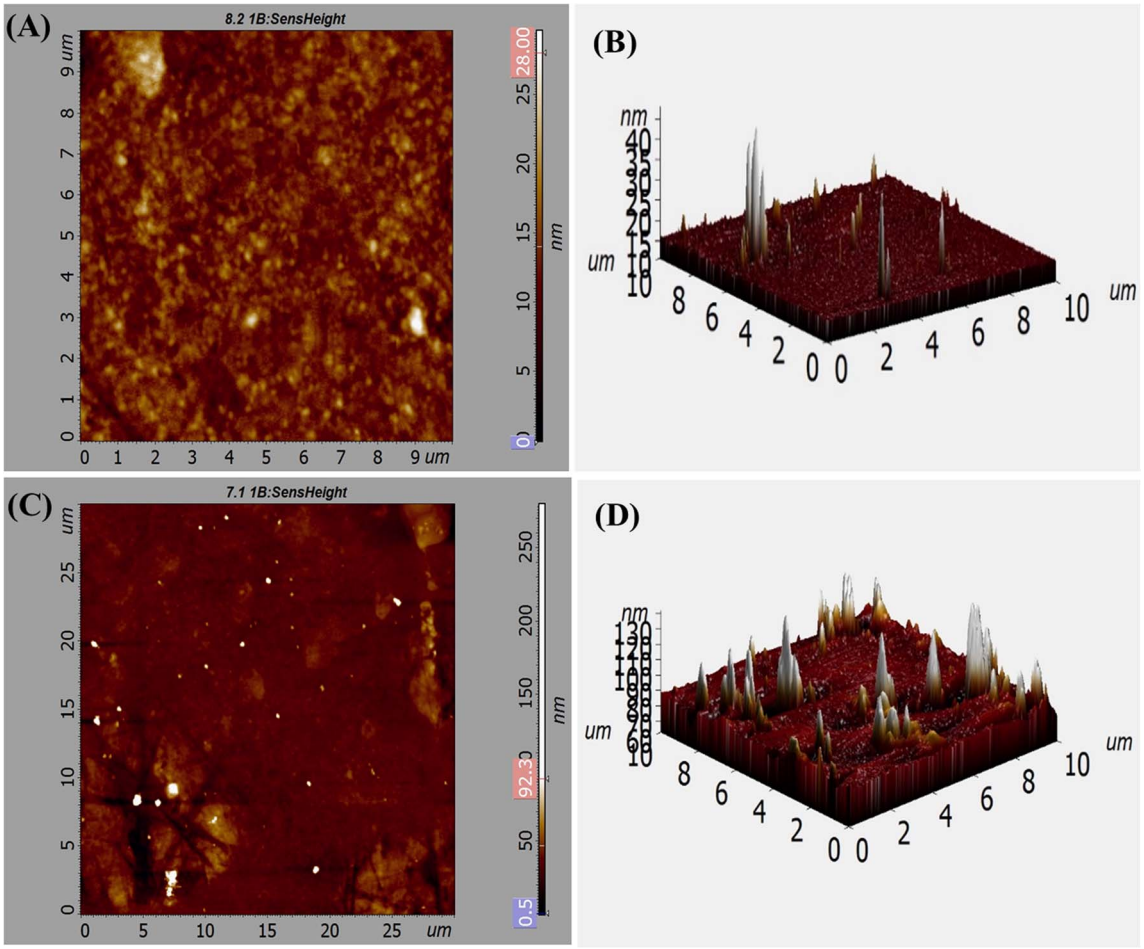

Fig. 5 2D and 3D AFM images of MCM-41(A & B) and MSNs–BBR (C & D).

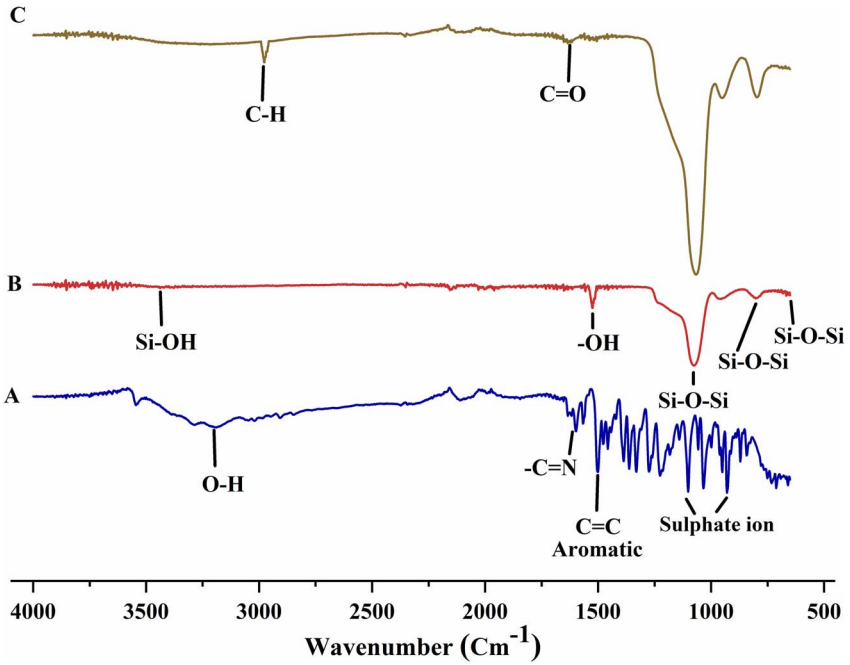

Fig. 6 FTIR spectrum of BBR (A), MCM-41 (B), and MSNs–BBR (C).

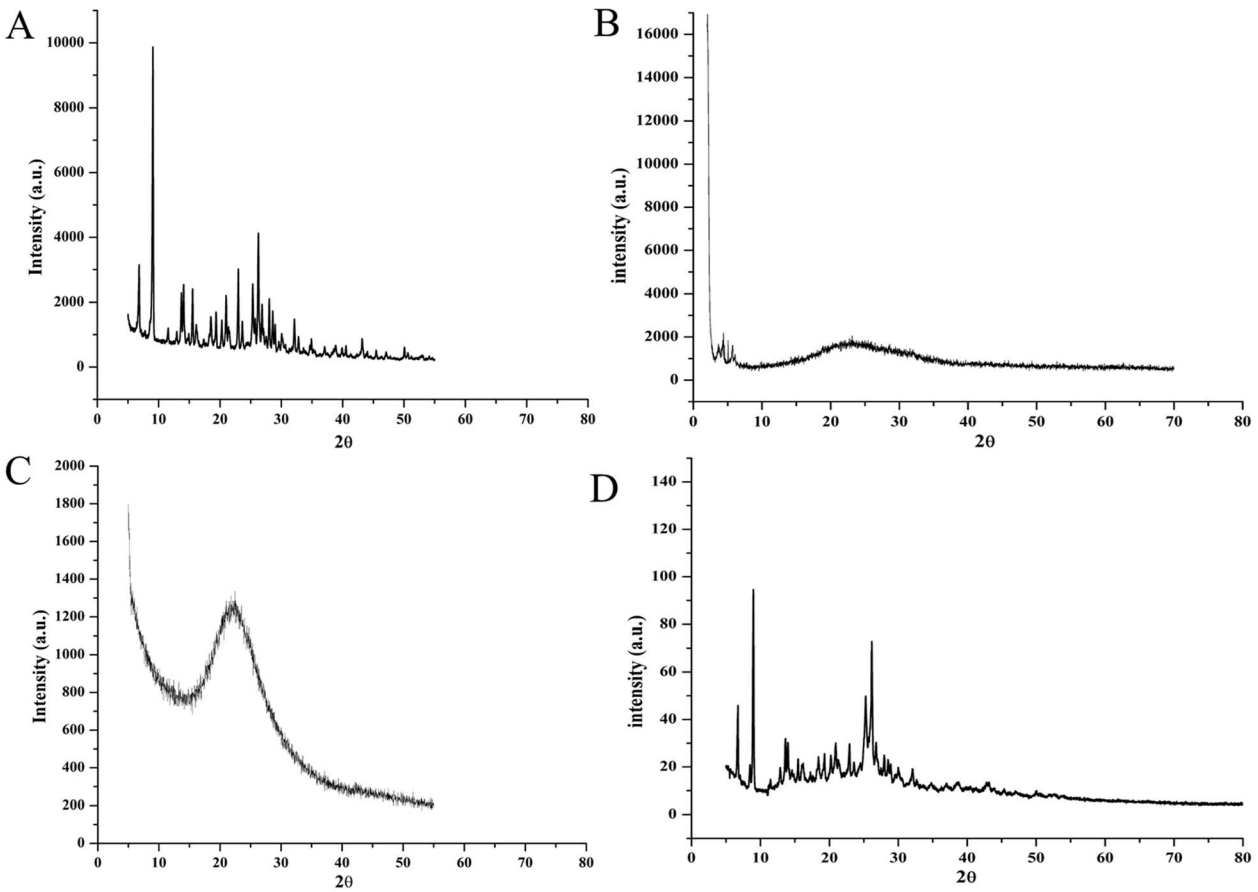

Fig. 7 X-ray diffractograms of (A) pure BBR, (B) MCM-41 (low angle), (C) MSNs–BBR, and (D) 1 : 1 w/w physically mixed MCM-41 and BBR.

3400 cm^{-1} (Fig. 6A). Absorption bands around 1107–1227 cm^{-1}, 1505 cm^{1}, 1602 cm^{-1}, and 3360 cm^{-1} in the FTIR spectrum of BBR are attributed to the presence of sulfate ions, aromatic C=C vibrations, –C=N stretching, and O–H stretching, respectively (Fig. 6B).[45] The structure of MCM-41 was retained after BBR loading. In MSNs–BBR, the peak position was slightly shifted with a minor decrease in intensity between 2000 and 1000 cm^{-1}. Further, the BBR peak at 3360 cm^{-1} was shifted to 3423 cm^{-1} in the spectrum of MSNs–BBR (Fig. 6C).[46]

The solubility of a chemical in its amorphous form is greater than in its crystalline form due to the larger Gibbs free energy. XRD analysis determines whether the tested material is crystalline or amorphous. Sharp peaks suggest a crystalline structure, while the absence of sharp peaks implies an amorphous surface.[47] Peaks at 2θ of 7.5, 9.1, 12.9, 16.2, 20.9, 25.4, and 30.1 in the XRD spectrum of BBR confirm its crystalline nature (Fig. 7A). MCM-41 showed diffractions at 2θ of 3.80, 4.43, and 5.72 (Fig. 7B). The disappearance of BBR peaks in the formulation spectrum shows amorphous dispersion of payload within the MCM-41 hexagonal channels (Fig. 7C). However, BBR peaks were not suppressed in 1 : 1 w/w physically mixed BBR and MCM-41 (Fig. 7D).

XPS analysis was done to make sure that BBR was loaded into MSNs and to find the desired elements in MCM-41, BBR, and MSNs–BBR. The O 1s and Si 2p spectra contained a single peak centred at 533.0 eV and 104.0 eV, respectively, indicating the presence of silicates.[48] N 1s spectra had a single peak centred at 399.0 eV, indicating the presence of basic nitrogen atoms.[49] Signals of Si, C, N, and O were detected in the survey spectrum of MSNs–BBR, indicating successful loading of BBR in MCM-41. XPS survey spectra for MCM-41, BBR, and MSNs–BBR are shown in Fig. 8. Individual characteristic peaks are shown in Fig. S1–S3 (ESI).†

BBR loading in MSNs was further evaluated by TGA. MCM-41 showed two weight loss regions between 24 °C and 148 °C, and 354 °C and 649 °C due to the loss of moisture from the silica surface and silanol condensation, respectively (Fig. 9A).[34] BBR showed four decomposition phases between 230 and 648 °C with 25.00% weight loss (destruction of the skeleton structure of BBR), at 230 °C with 11.55% weight loss (decomposition of BBR), between 105 °C and 175 °C with 0.45% weight loss (melting of BBR), and at 105 °C with 14.21% weight loss (loss of moisture) (Fig. 9B). MSNs–BBR showed weight loss regions between 24 °C and 205 °C (moisture loss and melting of BBR)

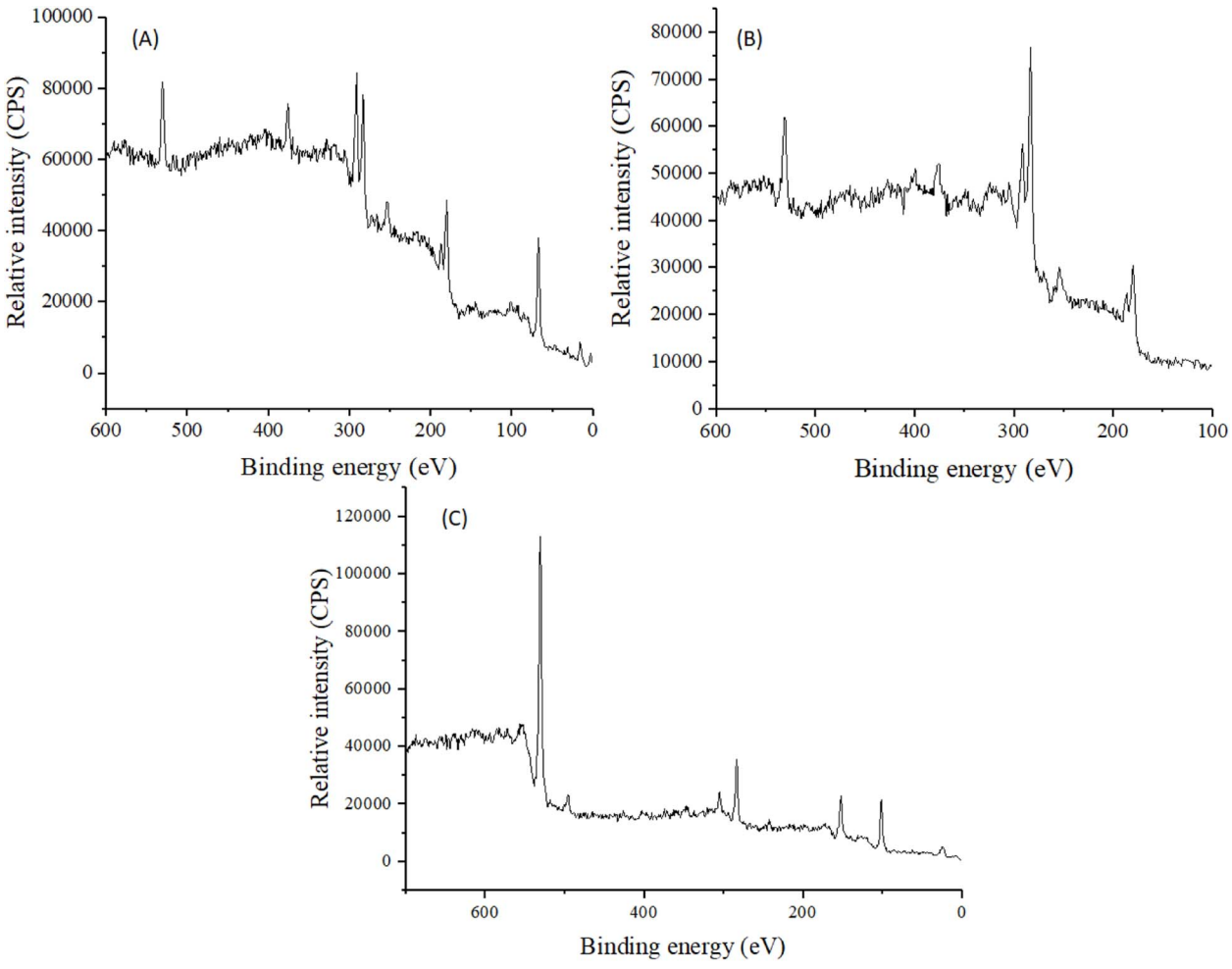

Fig. 8 XPS survey spectrum of MCM-41 (A), BBR (B), and MSNs–BBR (C).

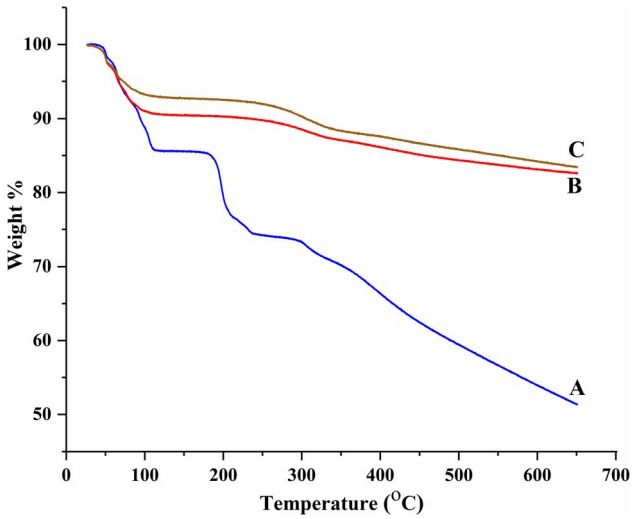

Fig. 9 TGA of (A) BBR, (B) MCM-41, and (C) MSNs–BBR.

and 205 °C and 649 °C (loss of the silanol group) (Fig. 9C). A 5.50% and 0.95% increase in weight loss was recorded in MSNs–BBR at 105 °C and between 325 and 448, respectively, indicating BBR loading. The rate of decomposition of pure BBR is fast as compared to the MCM-41 and MSNs–BBR. This demonstrates that the integration of BBR in MCM-41 can increase its thermal stability.

Nitrogen adsorption–desorption isotherms were measured to estimate the surface area and average pore diameter of MCM-41. This also helped in BBR loading confirmation and mesoporous structure characterization. MCM-41 samples displayed a type IV isotherm, which is a distinctive pattern of mesoporous materials according to the categorization of the IUPAC. This isotherm is characterized by a prominent capillary condensation step.[50] The results demonstrated uniform mesoporous channels and narrow pore size distribution. The pore volume and surface area of MCM-41 were 0.945 $cm^3\ g^{-1}$ and 49.780 $m^2\ g^{-1}$, respectively. However, the pore volume and surface area of MSNs–BBR were 0.054 $cm^3\ g^{-1}$ and 23.845 $m^2\ g^{-1}$, respectively (Fig. 10). The Barrett–Joyner–Halenda (BJH) method confirmed an average pore radius of 19.103 Å and 17.040 Å, respectively for MCM-41 and MSNs–BBR. The results indicated that the BBR loading decreased these mesoporosity parameters. This reducing tendency is attributed to BBR loading on the MCM-41.[51–53]

3.2. *In vitro* release

The in vitro release profile of BBR from pure BBR solution and MSNs–BBR formulation was estimated using the membrane-dialysis technique at pH 4.0 and pH 7.4 to simulate the pH of brain hippocampus and CSF, respectively (Fig. 11). MSNs–BBR showed a prolonged BBR release profile in both media. The dissolution profile showed a two-stage release profile. An initial fast BBR release was followed by a slow release up to 72 h. Initial fast release was due to the dissolution of the surface drug. Complete BBR was released from pure solution within 5 h of dissolution study. However, BBR release from MSNs–BBR prolonged till 72 h under both acidic and alkaline conditions suggesting stabilization of the drug in the polymer matrix.

For kinetic estimation, dissolution data were split into two stages, *i.e.*, (i) stage I (<8 h) and (ii) stage II (>8 h), and the best fit was selected based on the highest correlation coefficient (r^2) (Table 2). The r^2 value is a measure of how well the experimental *in vitro* drug release data fit the mathematical model, and higher r^2 values indicate a better fit. The BBR release from MSNs–BBR followed zero-order kinetics in both stages (r^2 values 0.9993, 0.9968 and 0.9979, 0.9977, respectively in both media). In Higuchi's model, the relationship between the cumulative amount of drug released and the square root of time ($Q = k\sqrt{t}$) is expected to be linear. Higuchi's plots of BBR loaded nanoparticles showed linearity (r^2 values 0.9991, 0.9966 and 0.9978, 0.9976, respectively in APB (pH 4.0) and PBS (pH 7.4) for stage I and stage II). The Higuchi plots show that the experimental data points are very close to the expected linear relationship. This means that Fickian diffusion is mainly responsible for the controlled release of BBR from the nanoparticles. If the slope (n)

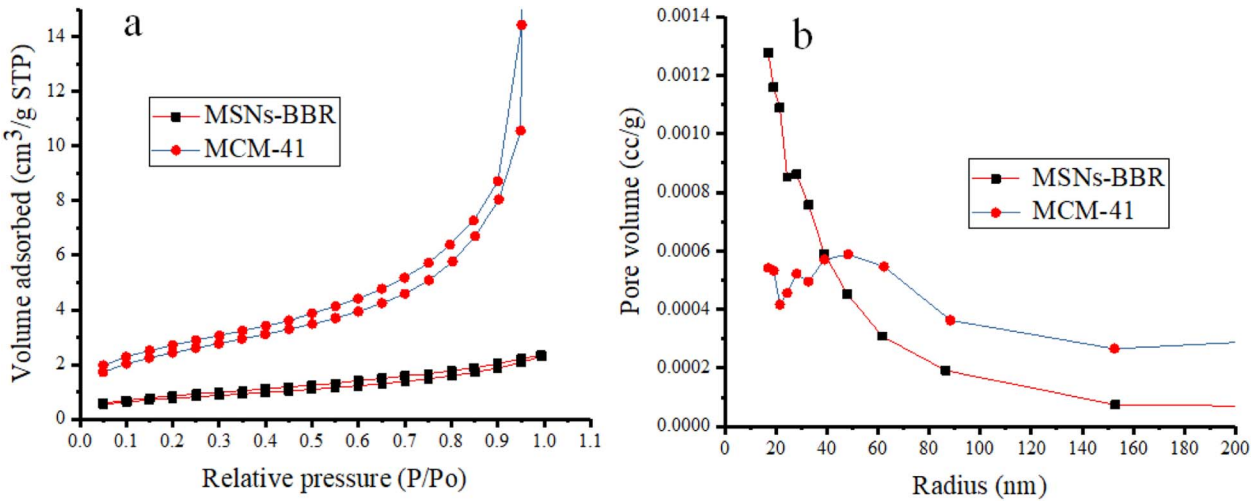

Fig. 10 Specific surface area (a) and porosity of MSNs (b).

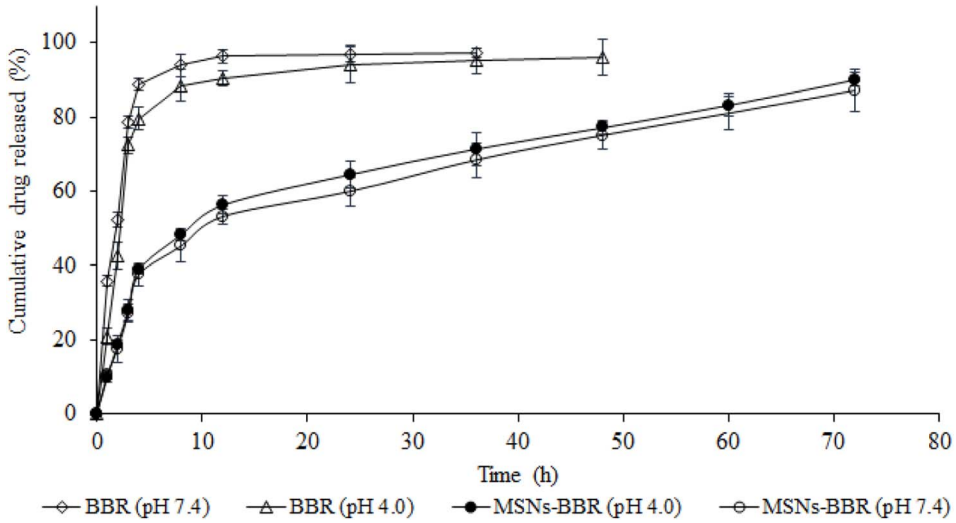

Fig. 11 BBR release from its pure solution (empty diamonds and empty triangles) and MSNs–BBR (filled circles and empty circles) at pH 4.0 and pH 7.4 at 37 ± 0.5 °C (mean ± SD, $n = 3$).

Table 2 Data of kinetic study of drug release from synthesized nanoparticles at pH 7.4 and pH 4.0

	pH 4.0					pH 7.4				
	Zero order	First order	Higuchi's model	Korsmeyer-Peppas' model		Zero order	First order	Higuchi's model	Korsmeyer-Peppas' model	
	r^2	r^2	r^2	r^2	n	r^2	r^2	r^2	r^2	n
Stage I (<8 h)	0.9993	0.9872	0.9991	0.9600	0.1692	0.9979	0.9911	0.9978	0.9682	0.1604
Stage II (>8 h)	0.9968	0.9622	0.9966	0.9853	0.0396	0.9977	0.9691	0.9976	0.9880	0.0437

value in Korsmeyer-Peppas' model lies between 0.43 and 0.85, the release profile follows a non-Fickian anomalous diffusion mechanism, and if the n value is >0.85, the release profile follows a swelling-controlled diffusion process. A super case II mode is followed if the n value is >1. Linearity of Korsmeyer-Peppas' plots confirmed BBR diffusion from MSNs–BBR (r^2 0.9600 to 0.9682 with slope values 0.1692 to 0.1604) for <8 h, indicating a simple or quasi-diffusion-controlled mechanism of drug release (Table 2). In a simple or quasi-diffusion-controlled mechanism, the drug molecules move through the matrix or core of the delivery system from areas of higher concentration to areas of lower concentration, following Fick's laws of diffusion. For quasi-diffusion-controlled release, the slope of the release curve is expected to follow Fick's law of diffusion. In mathematical terms, for quasi-diffusion-controlled release:

$$\frac{dM}{dt} = -D\frac{dC}{dx}$$

where dM/dt is the rate of drug release, D is the diffusion coefficient, and dC/dx is the concentration gradient.

The significance of this mechanism lies in its ability to provide controlled, sustained, and predictable drug release, leading to improved therapeutic outcomes. A similar pattern was observed after 8 h (stage II) of the dissolution study (r^2 0.9853–0.9880 with slope values between 0.0396 and 0.0437).

3.3. Analysis of diffusion of BBR molecules from the MCM-41 surfaces

A flat silica system was generated using alpha quartz structure by extending on both sides to give a small structure-like representation of silica slab. The first adsorbed drug layer was considered after MD simulation, as during the loading only the first adsorbed drug layer gets retained as it is tightly bound to the MCM-41 surface, whereas the rest of the molecules may be washed out. To the first adsorbed layer, water and salts were added to mimic the media. The drug release behavior from the MSNs–BBR particle surface can be assessed by analyzing the diffusion coefficient of BBR molecules. Fig. 12A and B show the pictorial visualization of the initial and final frame at 20 ns of BBR release from the plain MCM-41. To assess BBR release from the two surfaces, we calculated the diffusion coefficient, which demonstrated a relatively slower diffusion of BBR molecules from the plain MCM-41 surface.[24] The selection of a framework can exert a substantial influence on the loading and delivery of BBR. The impact of steric hindrance on the diffusion process of BBR molecules can explain the observed phenomenon.[54,55] Steric hindrance of the payload due to limited pore and channel sizes is likely to be highest in MCM-41. The greatest sphere diameter for channel diffusion is 19.103 Å, which is the average pore radius. Additionally, the BBR molecule experiences

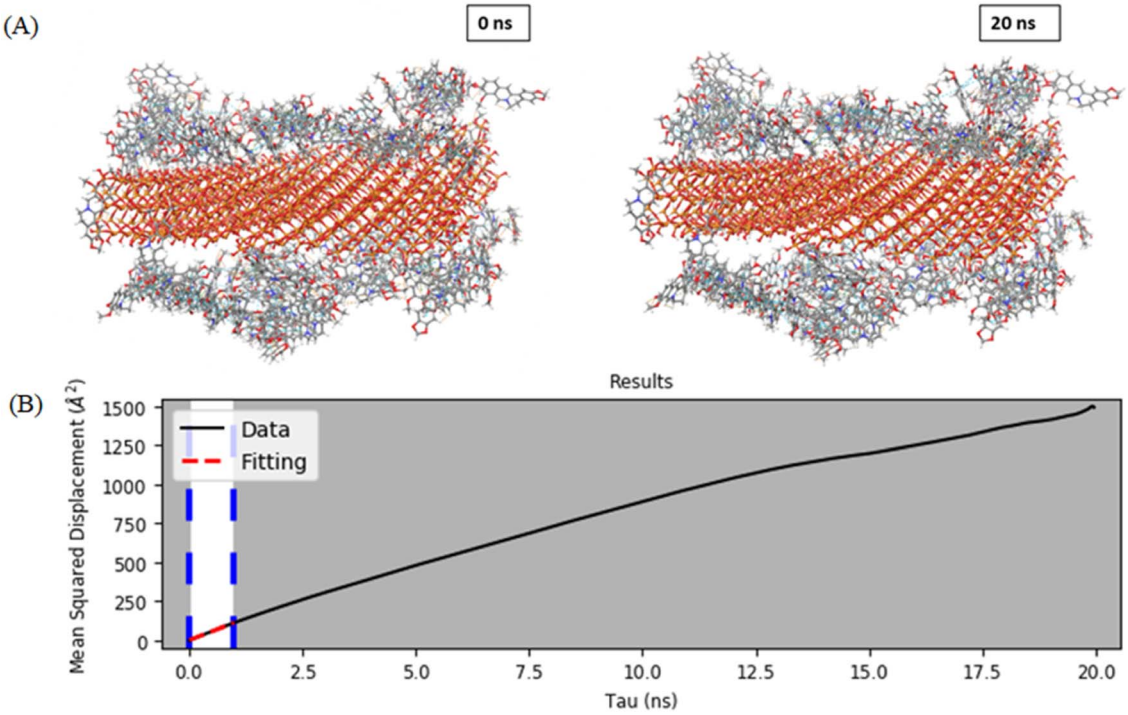

Fig. 12 Trajectory frames representing release of BBR molecules from the plain MCM-41 surface (brown indicates silicon atoms, red indicates oxygen atoms, and white indicates hydrogen atoms) (A). Diffusion coefficient of BBR molecules from the plain MCM-41 surface over 20 ns simulation (B).

a relatively tight fit with limited movement allowed within the channels. In phosphate buffer, BBR release is slower than in an acidic medium. This suggests that the intensity of BBR-framework interactions is pH-dependent, possibly because of pH affecting the framework's charge, the BBR molecule's charge, water molecules, or a combination of all three. The diffusion coefficient of BBR molecules from the plain MCM-41 surface was found to be 1.863×10^{-10} m^2 s^{-1}.

3.4. Hemolytic toxicity

The percentage of hemolysis in each sample was compared to distilled water (standard for 100% hemolysis). The hemocompatibility experiment revealed no statistically significant hemolysis when blood cells were exposed to the MSNs–BBR, pure BBR, and MCM-41 suspension (Fig. S4 – ESI file†). The hemolysis percentages were found to be $4.98 \pm 0.10\%$, $1.90 \pm 0.18\%$, and $4.30 \pm 0.21\%$, respectively. Hemolysis percentages below 5% suggest the safety of the substance for drug delivery.[9,36,56] Based on these findings, it can be inferred that the developed system may become a potential candidate for drug delivery applications.

3.5. Effect of BBR and MSNs–BBR on SH-SY-5Y cell proliferation

Cell viability assay was carried out to determine the cytotoxic effect of BBR and MSNs–BBR on SH-SY-5Y cells following 24 h of drug exposure. BBR and MSNs–BBR inhibited SH-SY-5Y cell proliferation in a dose-dependent manner. Cell viability decreased with an increase in BBR and MSNs–BBR concentrations. The cells exposed to 50 μg mL^{-1} of pure BBR and MSNs–BBR for 24 h showed reduced cell viability of ≈55.00% and 60.00%, respectively. This shows that BBR is more toxic than MSNs–BBR (Fig. 13).

3.6. Effect of BBR and MSNs–BBR on morphological changes in SH-SY-5Y cells

Phase-contrast microscopic images revealed that the BBR treatment initiated morphological changes in cells compared to

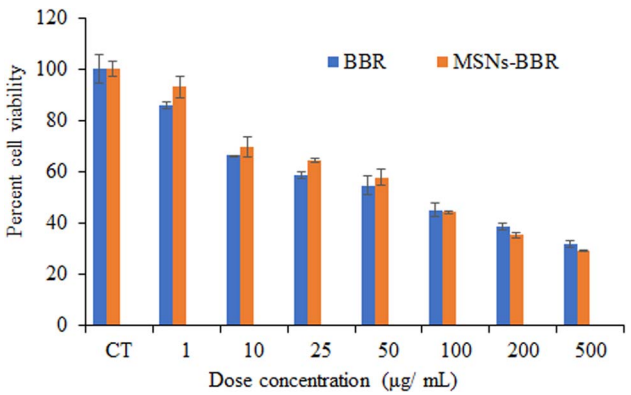

Fig. 13 Dose dependent effect on the proliferation of the neuroblastoma cell line. SH-SY-5Y cells were exposed to the indicated concentrations of mentioned compounds (1–500 μg mL^{-1}) and the cell viability was assayed using MTT as a substrate by taking absorbance at 570 nm.

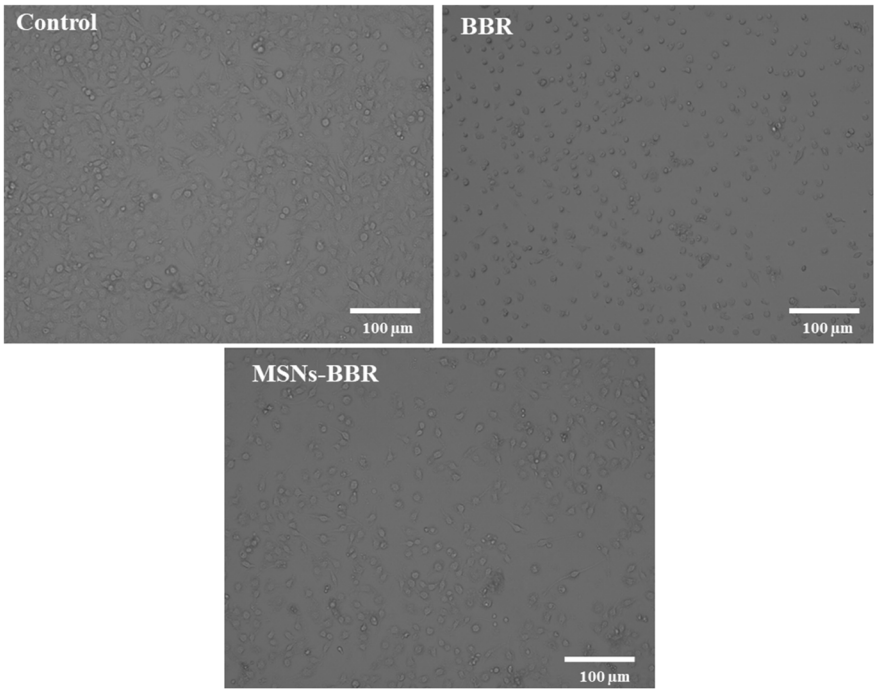

Fig. 14 Phase contrast microscopy images at 10× magnification showing morphological appearance of the neuroblastoma cell line (SH-SY-5Y cells), 24 h post-treatment with BBR and MSNs–BBR.

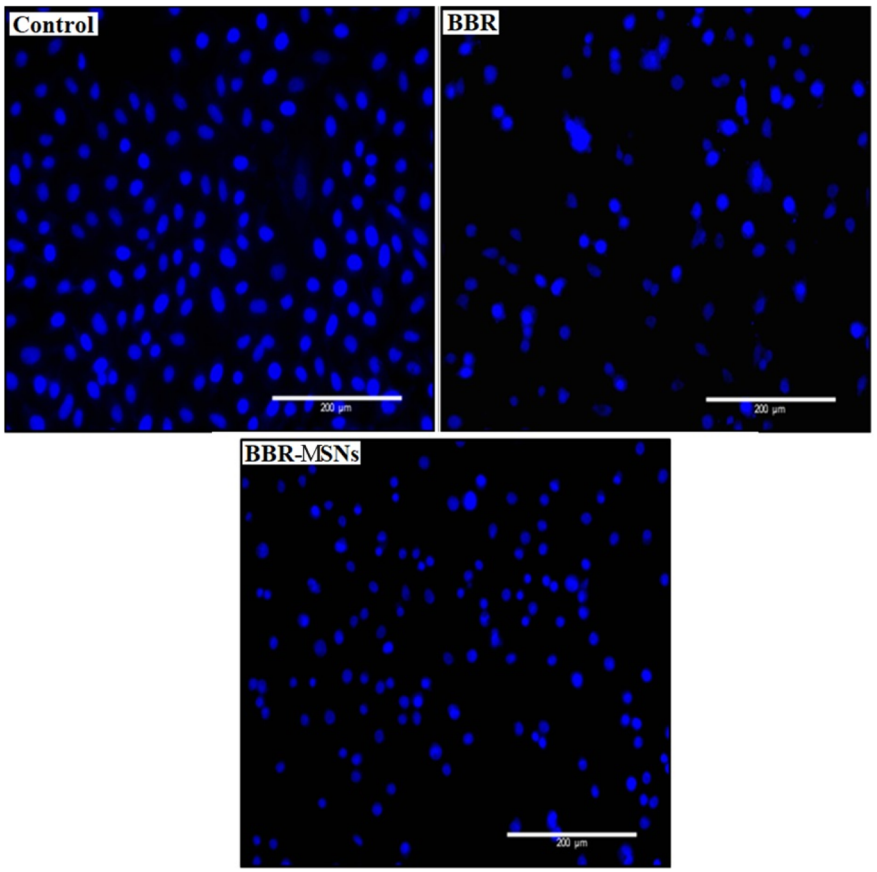

Fig. 15 Effect of BBR and MSNs–BBR on the morphological changes in the cell nucleus of the neuroblastoma cell line. Microscopic examination of SH-SY-5Y cells stained with DAPI after treatment with indicated concentration of drugs for 24 h and images were photographed at 20× magnification.

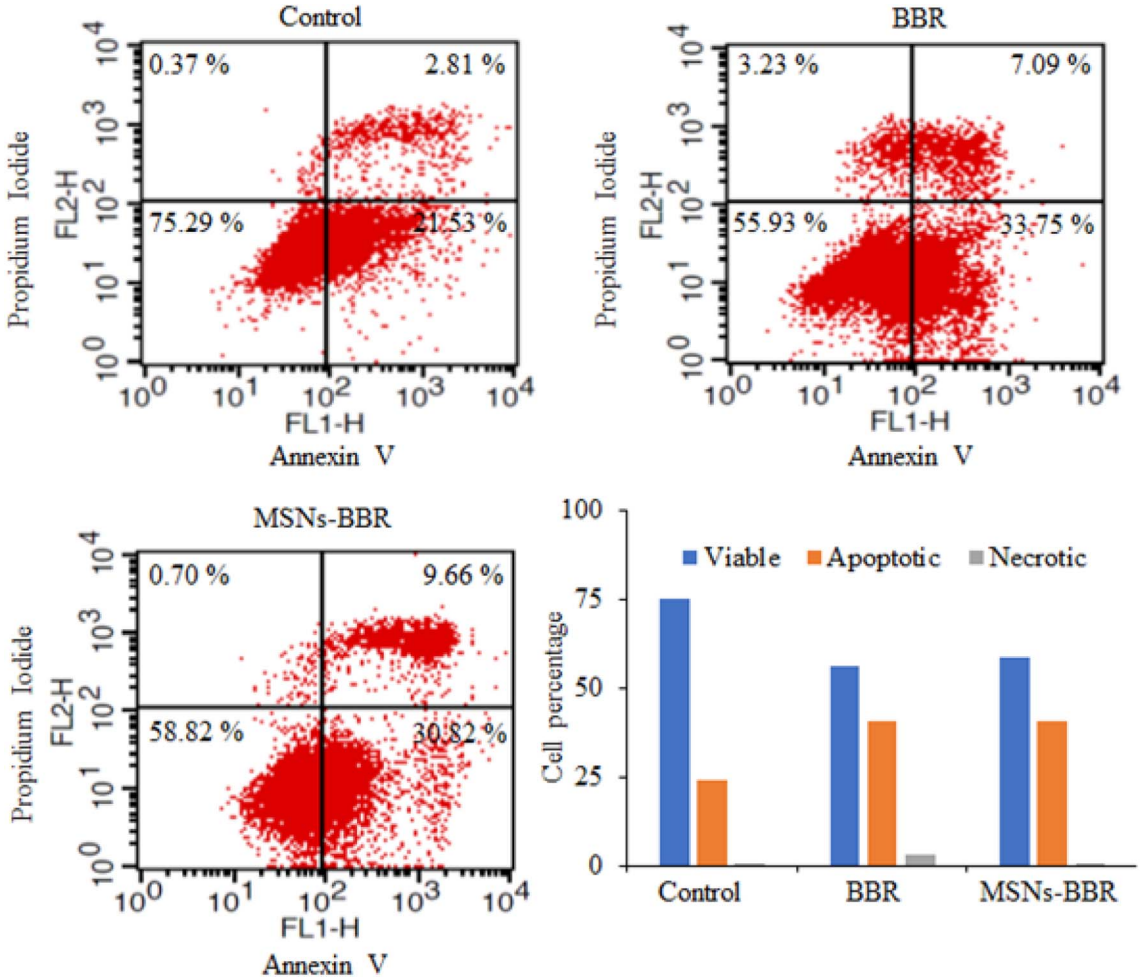

Fig. 16 Flow cytometric analysis of SH-SY-5Y cells stained with Alexafluor 488 conjugated annexin V antibody after treatment to discriminate the percentage of viable, early apoptotic, late apoptotic, and necrotic cells in different quadrants.

the control. An increase in apoptotic cells and a decrease in viable cells were recorded after treatment with BBR and MSNs–BBR (Fig. 14).

3.7. Effect of BBR and MSNs–BBR on nuclear changes in SH-SY-5Y cells

Nuclear staining was carried out to observe the nuclear changes after treatment with BBR and MSNs–BBR. Round or oval nuclei were observed in control. However, fragmented cell nuclei and nuclear apoptotic bodies were observed in the cases of BBR and MSNs–BBR treated cells (Fig. 15).

3.8. Effect of BBR and MSNs–BBR on apoptosis in SH-SY-5Y cells

Flow cytometry was used to quantify the rate of viable, apoptotic, and necrotic cells. In control, the percentage of live and apoptotic cells was found to be 75.29% and 24.34%, respectively. BBR treatment reduced the percentage of live and apoptotic cells to 55.93% and 40.84%, respectively. MSNs–BBR increased the percentage of live cells from 55.93% to 58.82% and decreased the percentage of apoptotic cells from 40.84% to 40.48%. It indicated the potential of MSNs–BBR in preventing apoptotic processes and restoring cellular viability (Fig. 16).

3.9. Effect of BBR and MSNs–BBR on mitochondrial membrane potential in SH-SY-5Y cells

We investigated the impact of BBR and MSNs–BBR treatment on $\Delta\Psi$ by assessing mitochondrial activity in treated and untreated cells using the fluorochrome JC-1, which accumulates in the mitochondria based on its membrane potential. When the membrane potential is low, the JC-1 monomer emits green fluorescence. Healthy mitochondria contain JC-1 in their aggregated form, resulting in red to orange fluorescence. The control cells displayed red fluorescence, while an enhancement in green fluorescence intensity was noted following treatment with BBR and MSNs–BBR. BBR causes depolarization of the $\Delta\Psi$, indicated by increased JC-1 green fluorescence compared to control cells. In contrast, MSNs–BBR reduced depolarization of the $\Delta\Psi$, represented by higher JC-1 red fluorescence compared to BBR treated cells. The data indicate that MSNs–BBR reduce the depolarization of mitochondria more effectively than BBR, hence preventing apoptosis and restoring the $\Delta\Psi$ (Fig. 17).

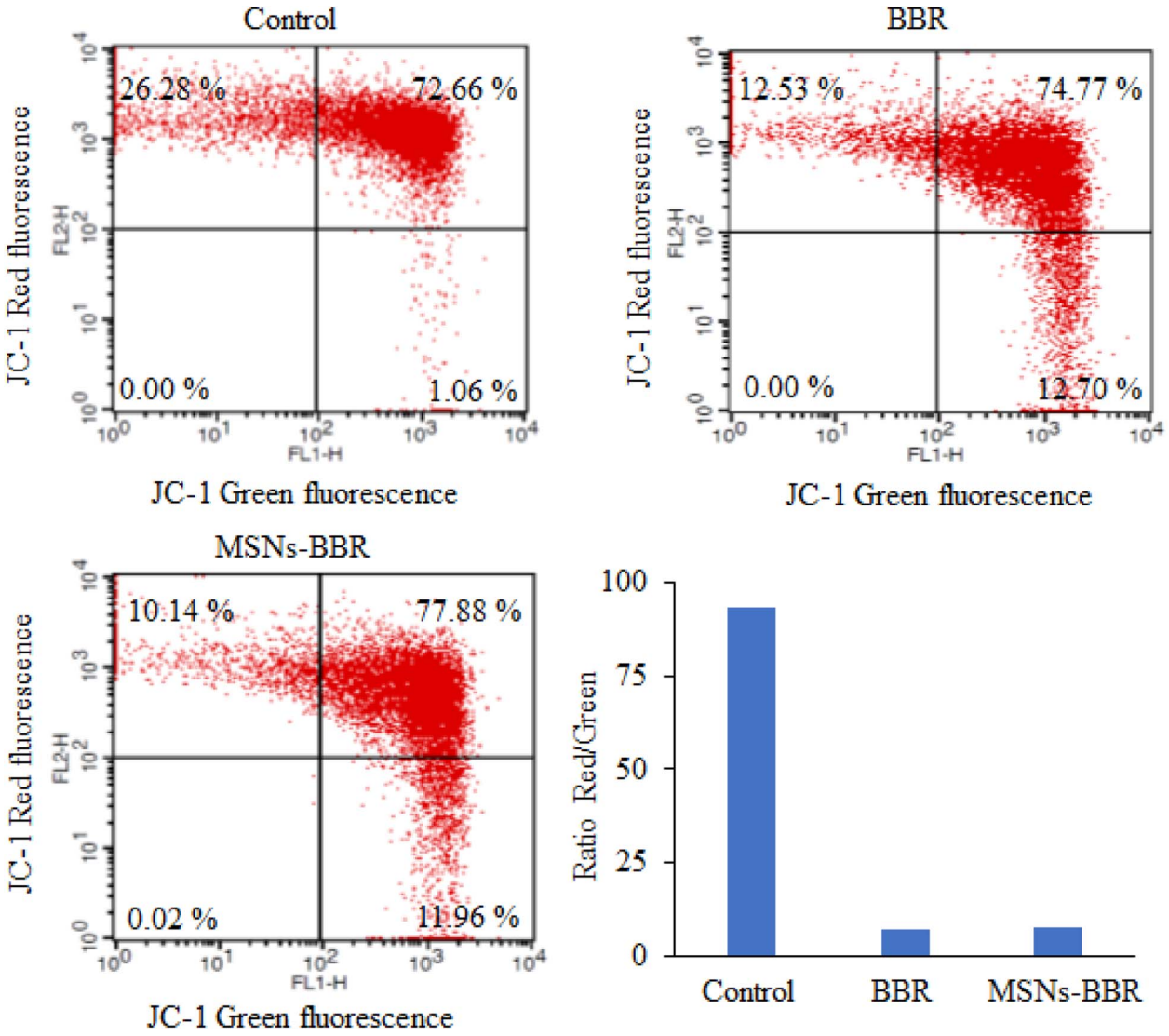

Fig. 17 BBR causes a decrease in the mitochondrial membrane potential ($\Delta\Psi$), resulting in increased JC-1 green fluorescence relative to the control cells. MSNs–BBR decreased $\Delta\Psi$ depolarization compared to cells treated with BBR alone, resulting in increased JC-1 red fluorescence.

4 Conclusions

Nanoparticles had a high BBR loading and entrapment efficiency despite their small size. Prolonged BBR release following the diffusion process was confirmed by molecular dynamics simulation study. TGA analysis confirmed BBR loading. Increased apoptotic cells and decreased viable cells were noticed in phase-contrast microscopic images. Fragmented cell nuclei and nuclear apoptotic bodies were recorded in SH-SY-5Y cells stained with DAPI. Flow cytometric analysis of formulation treated SH-SY-5Y cells showed restoration of cellular viability, membrane potential and improvement of neuronal health.

Author contributions

Anurag Kumar Singh: methodology, data curation, validation, formal analysis, investigation, writing – original draft, visualization. Snigdha Singh: methodology, data curation, validation, formal analysis, investigation, writing – original draft, visualization. Tarun Minocha: methodology, software, investigation, writing – original draft Sanjeev Kumar Yadav: validation, writing – review & editing, visualization. Reema Narayan: conceptualization, software, writing – review & editing, visualization. Usha Yogendra Nayak: conceptualization, software, validation, writing – review & editing, visualization. Rajendra Awasthi: methodology, validation, investigation, writing – original draft, writing – review & editing, supervision Santosh Kumar Singh: conceptualization, methodology, validation, writing – review & editing, supervision.

Conflicts of interest

There are no conflicts to declare.

Acknowledgements

The authors are thankful to the Institute of Eminence (IOE), Banaras Hindu University, Center of Experimental Medicine

and Surgery, Institute of Medical Sciences, Banaras Hindu University, Varanasi, Central Discovery Centre (CDC), Banaras Hindu University, Varanasi and Central Instrument Facility Center, Indian Institute of Technology, Banaras Hindu University, Varanasi for providing research facilities.

References

1 D. W. Coon and A. Gómez-Morales, Modifiable Risk Factors for Brain Health and Dementia and Opportunities for Intervention: A Brief Review, *Clin. Gerontol.*, 2023, **46**(2), 143–154.

2 V. L. Feigin, E. Nichols, T. Alam, M. S. Bannick, E. Beghi, N. Blake, W. J. Culpepper, E. R. Dorsey, A. Elbaz, R. G. Ellenbogen and J. L. Fisher, Global, regional, and national burden of neurological disorders, 1990–2016: a systematic analysis for the Global Burden of Disease Study 2016, *Lancet Neurol.*, 2019, **18**(5), 459–480.

3 A. K. Singh, S. S. Singh, A. S. Rathore, S. P. Singh, G. Mishra, R. Awasthi, S. K. Mishra, V. Gautam and S. K. Singh, Lipid-coated MCM-41 mesoporous silica nanoparticles loaded with berberine improved inhibition of acetylcholine esterase and amyloid formation, *ACS Biomater. Sci. Eng.*, 2021, **7**(8), 3737–3753.

4 S. Mendiratta, M. Hussein, H. A. Nasser and A. A. Ali, Multidisciplinary role of mesoporous silica nanoparticles in brain regeneration and cancers: From crossing the blood–brain barrier to treatment, *Part. Part. Syst. Charact.*, 2019, **36**(9), 1900195.

5 G. C. Terstappen, A. H. Meyer, R. D. Bell and W. Zhang, Strategies for delivering therapeutics across the blood–brain barrier, *Nat. Rev. Drug Discovery*, 2021, **20**(5), 362–383.

6 M. J. Mitchell, M. M. Billingsley, R. M. Haley, M. E. Wechsler, N. A. Peppas and R. Langer, Engineering precision nanoparticles for drug delivery, *Nat. Rev. Drug Discovery*, 2021, **20**(2), 101–124.

7 Y. Wang, Q. Zhao, N. Han, L. Bai, J. Li, J. Liu, E. Che, L. Hu, Q. Zhang, T. Jiang and S. Wang, Mesoporous silica nanoparticles in drug delivery and biomedical applications, *Nanomed. Nanotechnol. Biol. Med.*, 2015, **11**(2), 313–327.

8 X. Jiang, X. Tang, L. Tang, B. Zhang and H. Mao, Synthesis and formation mechanism of amorphous silica particles via sol–gel process with tetraethylorthosilicate, *Ceram. Int.*, 2019, **45**(6), 7673–7680.

9 A. E. LaBauve, T. E. Rinker, A. Noureddine, R. E. Serda, J. Y. Howe, M. B. Sherman, A. Rasley, C. J. Brinker, D. Y. Sasaki and O. A. Negrete, Lipid-coated mesoporous silica nanoparticles for the delivery of the ML336 antiviral to inhibit encephalitic alphavirus infection, *Sci. Rep.*, 2018, **8**(1), 13990.

10 S. P. Fortis, A. Batrinou, H. T. Georgatzakou, I. Tsamesidis, G. Alvanidis, E. G. Papageorgiou, K. Stamoulis, D. Gkiliopoulos, G. K. Pouroutzidou, A. Theocharidou and E. Kontonasaki, Effect of silica-based mesoporous nanomaterials on human blood cells, *Chem.-Biol. Interact.*, 2024, **387**, 110784.

11 Y. Feng, Y. Cao, Z. Qu, T. I. Janjua and A. Popat, Virus-like silica nanoparticles improve permeability of macromolecules across the blood–brain barrier *in vitro*, *Pharmaceutics*, 2023, **15**(9), 2239.

12 G. Mishra, R. Awasthi, A. K. Singh, S. Singh, S. K. Mishra, S. K. Singh and M. K. Nandi, Intranasally Co-administered Berberine and Curcumin Loaded in Transfersomal Vesicles Improved Inhibition of Amyloid Formation and BACE-1, *ACS Omega*, 2022, **7**(47), 43290–43305.

13 Y. T. Liu, H. P. Hao, H. G. Xie, L. Lai, Q. Wang, C. X. Liu and G. J. Wang, Extensive intestinal first-pass elimination and predominant hepatic distribution of berberine explain its low plasma levels in rats, *Drug Metab. Dispos.*, 2010, **38**(10), 1779–1784.

14 W. Chen, Y. Q. Miao, D. J. Fan, S. S. Yang, X. Lin, L. K. Meng and X. Tang, Bioavailability study of berberine and the enhancing effects of TPGS on intestinal absorption in rats, *AAPS PharmSciTech*, 2011, **12**, 705–711.

15 A. T. Nies, E. Herrmann, M. Brom and D. Keppler, Vectorial transport of the plant alkaloid berberine by double-transfected cells expressing the human organic cation transporter 1 (OCT1, SLC22A1) and the efflux pump MDR1 P-glycoprotein (ABCB1), *Naunyn-Schmiedeberg's Arch. Pharmacol.*, 2008, **376**, 449–461.

16 D. S. Kohane and R. Langer, Biocompatibility and drug delivery systems, *Chem. Sci.*, 2010, **1**(4), 441–446.

17 W. Stöber, A. Fink and E. Bohn, Controlled growth of monodisperse silica spheres in the micron size range, *J. Colloid Interface Sci.*, 1968, **26**(1), 62–69.

18 Y. Yang, W. Song, A. Wang, P. Zhu, J. Fei and J. Li, Lipid coated mesoporous silica nanoparticles as photosensitive drug carriers, *Phys. Chem. Chem. Phys.*, 2010, **12**(17), 4418–4422.

19 Y. Shi, A. Wan, Y. Shi, Y. Zhang and Y. Chen, Experimental and mathematical studies on the drug release properties of aspirin loaded chitosan nanoparticles, *BioMed Res. Int.*, 2014, **2014**, 613619.

20 S. Zhang, M. Perez-Page, K. Guan, E. Yu, J. Tringe, R. H. Castro, R. Faller and P. Stroeve, Response to extreme temperatures of mesoporous silica MCM-41: porous structure transformation simulation and modification of gas adsorption properties, *Langmuir*, 2016, **32**(44), 11422–11431.

21 A. Olejnik and J. Goscianska, On the importance of physicochemical parameters of copper and aminosilane functionalized mesoporous silica for hydroxychloroquine release, *Mater. Sci. Eng. C*, 2021, **130**, 112438.

22 H. Ohkawa, N. Ohishi and K. Yagi, Assay for lipid peroxides in animal tissues by thiobarbituric acid reaction, *Anal. Biochem.*, 1979, **95**(2), 351–358.

23 V. R. Malipeddi, K. Dua and R. Awasthi, Development and characterization of solid dispersion-microsphere controlled release system for poorly water-soluble drug, *Drug Delivery Transl. Res.*, 2016, **6**, 540–550.

24 R. Narayan, S. Gadag, S. Garg and U. Y. Nayak, Understanding the effect of functionalization on loading capacity and release of drug from mesoporous silica

nanoparticles: a computationally driven study, *ACS Omega*, 2022, **7**(10), 8229–8245.

25 A. K. Singh, A. Gothwal, S. Rani, M. Rana, A. K. Sharma, A. K. Yadav and U. Gupta, Dendrimer donepezil conjugates for improved brain delivery and better *in vivo* pharmacokinetics, *ACS Omega*, 2019, **4**(3), 4519–4529.

26 A. K. Singh, S. K. Mishra, G. Mishra, A. Maurya, R. Awasthi, M. K. Yadav, N. Atri, P. K. Pandey and S. K. Singh, Inorganic clay nanocomposite system for improved cholinesterase inhibition and brain pharmacokinetics of donepezil, *Drug Dev. Ind. Pharm.*, 2020, **46**(1), 8–19.

27 T. Minocha, M. Das, V. Rai, S. S. Verma, N. Awasthee, S. C. Gupta, C. Haldar and S. K. Yadav, Melatonin induces apoptosis and cell cycle arrest in cervical cancer cells via inhibition of NF-κB pathway, *Inflammopharmacol.*, 2022, **30**, 1411–1429.

28 D. Moutinho, S. Veiga and J. R. Requena, Human VGF-derived antidepressant neuropeptide TLQP62 promotes SH-SY5Y neurite outgrowth, *J. Mol. Neurosci.*, 2020, **70**, 1293–1302.

29 G. Yordanov, R. Skrobanska and M. Petkova, Poly (butyl cyanoacrylate) nanoparticles stabilised with poloxamer 188: particle size control and cytotoxic effects in cervical carcinoma (HeLa) cells, *Chem. Pap.*, 2016, **70**(3), 365–374.

30 V. Rai, S. K. Aggarwal, S. S. Verma, N. Awasthee, A. Dhasmana, S. Aggarwal, S. N. Das, M. S. Nair, S. Yadav and S. C. Gupta, Epoxyazadiradione exhibit activities in head and neck squamous cell carcinoma by targeting multiple pathways, *Apoptosis*, 2020, **25**, 763–782.

31 S. S. Verma, V. Rai, N. Awasthee, A. Dhasmana, D. S. Rajalaksmi, M. S. Nair and S. C. Gupta, Isodeoxyelephantopin, a sesquiterpene lactone induces ROS generation, suppresses NF-κB activation, modulates LncRNA expression and exhibit activities against breast cancer, *Sci. Rep.*, 2019, **9**(1), 17980.

32 H. Refai, D. Hassan and R. Abdelmonem, Development and characterization of polymer-coated liposomes for vaginal delivery of sildenafil citrate, *Drug Delivery*, 2017, **24**(1), 278–288.

33 N. Raval, R. Maheshwari, D. Kalyane, S. R. Youngren-Ortiz, M. B. Chougule and R. K. Tekade, Importance of physicochemical characterization of nanoparticles in pharmaceutical product development, In.*Basic fundamentals of drug delivery*, Academic Press, 2019, vol. 1, pp. 369–400.

34 S. Saroj and S. J. Rajput, Etoposide encapsulated functionalized mesoporous silica nanoparticles: Synthesis, characterization and effect of functionalization on dissolution kinetics in simulated and biorelevant media, *J. Drug Delivery Sci. Technol.*, 2018, **44**, 27–40.

35 T. Govender, S. Stolnik, M. C. Garnett, L. Illum and S. S. Davis, PLGA nanoparticles prepared by nanoprecipitation: drug loading and release studies of a water soluble drug, *J. Controlled Release*, 1999, **57**(2), 171–185.

36 P. K. Pandey, A. K. Sharma, S. Rani, G. Mishra, G. Kandasamy, A. K. Patra, M. Rana, A. K. Sharma, A. K. Yadav and U. Gupta, MCM-41 nanoparticles for brain delivery: better choline-esterase and amyloid formation inhibition with improved kinetics, *ACS Biomater. Sci. Eng.*, 2018, **4**(8), 2860–2869.

37 Z. Li, Y. Zhang, K. Zhang, Z. Wu and N. Feng, Biotinylated-lipid bilayer coated mesoporous silica nanoparticles for improving the bioavailability and anti-leukaemia activity of Tanshinone IIA, *Artif. Cells, Nanomed., Biotechnol.*, 2018, **46**(1), 578–587.

38 N. Ž. Knežević and J. O. Durand, Targeted treatment of cancer with nanotherapeutics based on mesoporous silica nanoparticles, *ChemPlusChem*, 2015, **80**(1), 26–36.

39 I. M. Joni, R. Balgis, T. Ogi, T. Iwaki and K. Okuyama, Surface functionalization for dispersing and stabilizing hexagonal boron nitride nanoparticle by bead milling, *Colloids Surf., A*, 2011, **388**(1–3), 49–58.

40 P. R. Lockman, J. M. Koziara, R. J. Mumper and D. D. Allen, Nanoparticle surface charges alter blood–brain barrier integrity and permeability, *J. Drug Targeting*, 2004, **12**(9–10), 635–641.

41 P. Decuzzi, B. Godin, T. Tanaka, S. Y. Lee, C. Chiappini, X. Liu and M. J. Ferrari, Size and shape effects in the biodistribution of intravascularly injected particles, *J. Controlled Release*, 2010, **141**(3), 320–327.

42 J. Kreuter, T. Hekmatara, S. Dreis, T. Vogel, S. Gelperina and K. Langer, Covalent attachment of apolipoprotein AI and apolipoprotein B-100 to albumin nanoparticles enables drug transport into the brain, *J. Controlled Release*, 2007, **118**(1), 54–58.

43 N. Alharbi, S. Teerakanok, J. D. Satterthwaite, R. Giordano and N. Silikas, Quantitative nano-mechanical mapping AFM-based method for elastic modulus and surface roughness measurements of model polymer infiltrated ceramics, *Dent. Mater.*, 2022, **38**(6), 935–945.

44 U. Maver, T. Velnar, M. Gaberšček, O. Planinšek and M. Finšgar, Recent progressive use of atomic force microscopy in biomedical applications, *TrAC, Trends Anal. Chem.*, 2016, **80**, 96–111.

45 R. Solanki, K. Patel and S. Patel, Bovine serum albumin nanoparticles for the efficient delivery of berberine: Preparation, characterization and *in vitro* biological studies, *Colloids Surf., A*, 2021, **608**, 125501.

46 S. K. Battu, M. A. Repka, S. Maddineni, A. G. Chittiboyina, M. A. Avery and S. Majumdar, Physicochemical characterization of berberine chloride: a perspective in the development of a solution dosage form for oral delivery, *AAPS PharmSciTech*, 2010, **11**, 1466–1475.

47 S. A. Ghodke, U. Maheshwari, S. Gupta, S. H. Sonawane and B. A. Bhanvase, Nanomaterials for adsorption of pollutants and heavy metals: Introduction, mechanism, and challenges, In.*Handbook of Nanomaterials for Wastewater Treatment*, Elsevier, 2021, pp. 343–366.

48 S. Shen, J. Chen, R. T. Koodali, Y. Hu, Q. Xiao, J. Zhou, X. Wang and L. Guo, Activation of MCM-41 mesoporous silica by transition-metal incorporation for photocatalytic hydrogen production, *Appl. Catal., B*, 2014, **150**, 138–146.

49 F. Zhang, M. Zhang, X. Zheng, S. Tao, Z. Zhang, M. Sun, Y. Song, J. Zhang, D. Shao, K. He and J. Li, Berberine-based carbon dots for selective and safe cancer theranostics, *RSC Adv.*, 2018, **8**(3), 1168–1173.

50 M. S. Salam, M. A. Betiha, S. A. Shaban, A. M. Elsabagh and R. M. Abd El-Aal, Synthesis and characterization of MCM-41-supported nano zirconia catalysts, *Egypt. J. Pet.*, 2015, **24**(1), 49–57.

51 J. Yue, Z. Wang, D. Shao, Z. Chang, R. Hu, L. Li, S. Z. Luo and W. F. Dong, Cancer cell membrane-modified biodegradable mesoporous silica nanocarriers for berberine therapy of liver cancer, *RSC Adv.*, 2018, **8**(70), 40288–40297.

52 G. Kuang, Q. Zhang, S. He and Y. Liu, Curcumin-loaded PEGylated mesoporous silica nanoparticles for effective photodynamic therapy, *RSC Adv.*, 2020, **10**(41), 24624–24630.

53 L. Usgodaarachchi, C. Thambiliyagodage, R. Wijesekera and M. G. Bakker, Synthesis of mesoporous silica nanoparticles derived from rice husk and surface-controlled amine functionalization for efficient adsorption of methylene blue from aqueous solution, *Curr. Res. Green Sustainable Chem.*, 2021, **4**, 100116.

54 A. J. Wise, J. S. Sefy, E. Barbu, A. J. O'Malley, S. M. van der Merwe and P. A. Cox, Zero-order and prolonged release of atenolol from microporous FAU and BEA zeolites, and mesoporous MCM-41: Experimental and theoretical investigations, *J. Controlled Release*, 2020, **327**, 140–149.

55 A. Datt, I. El-Maazawi and S. C. Larsen, Aspirin loading and release from MCM-41 functionalized with aminopropyl groups via co-condensation or postsynthesis modification methods, *J. Phys. Chem. C*, 2012, **116**(34), 18358–18366.

56 K. Amin and R. M. Dannenfelser, *In vitro* hemolysis: guidance for the pharmaceutical scientist, *J. Pharm. Sci.*, 2006, **95**(6), 1173–1176.